

Turbulence in electromagnetically driven Keplerian flows

M. Vernet^{1,†}, M. Pereira², S. Fauve¹ and C. Gissinger^{1,3}

¹Laboratoire de Physique de l'École Normale Supérieure, CNRS, PSL Research University, Sorbonne Université, Université de Paris, F-75005 Paris, France

²Arts et Métiers Institute of Technology, CNAM, LIFSE, HESAM University, F-75013 Paris, France

³Institut Universitaire de France (IUF), Paris, France

(Received 16 March 2021; revised 1 June 2021; accepted 8 July 2021)

The flow of an electrically conducting fluid in a thin disc under the action of an azimuthal Lorentz force is studied experimentally. At small forcing, the Lorentz force is balanced by either viscosity or inertia, yielding quasi-Keplerian velocity profiles. For very large current I and moderate magnetic field B , we observe a new regime, fully turbulent, which exhibits large fluctuations and a Keplerian mean rotation profile $\Omega \sim \sqrt{IB}/r^{3/2}$, where r is the distance from the axis. In this turbulent regime, the dynamics is typical of thin layer turbulence, characterized by a direct cascade of energy towards the small scales and an inverse cascade to large scales. Finally, at very large magnetic field, this turbulent flow bifurcates to a quasi-bidimensional turbulent flow involving the formation of a large scale condensate in the horizontal plane. These results are well understood as resulting from an instability of the Bödewadt–Hartmann layers at large Reynolds number and discussed in the framework of similar astrophysical flows.

Key words: transition to turbulence, MHD turbulence, boundary layer stability

1. Background

Since the pioneering work of Hartmann (Hartmann & Lazarus 1937) on electromagnetic conduction pumps, several works have been devoted to the study of flows of liquid metals driven by a stationary electromagnetic force. Experimentally, it is usually easier to study this problem in a cylindrical geometry, in which the flow is driven in the azimuthal direction under the effect of an axial magnetic field and the injection of a radial current. Because of the relatively homogeneous and delocalized forcing, this configuration is also advantageous over other set-ups when it comes to generate turbulent rotating flows.

In 1965, Hunt (1965) proposed one of the first theoretical studies of a magnetohydrodynamic (MHD) flow in the presence of conductive walls and deduced a

† Email address for correspondence: marlone.vernet@phys.ens.fr

theoretical expression for electrically driven flows. A first experimental confirmation of this theory was obtained in 1971 by Baylis (1971) and Baylis & Hunt (1971), in a laboratory experiment using mercury. By imposing a magnetic field strong enough to inhibit inertial effects, the authors confirmed the linear dependence of the flow with the applied current I . Later, Tabeling & Chabrierie (1981) proposed a new theoretical approach by looking at the recirculation likely to occur when the external field is not too strong. They found that a secondary flow involving no inertial effects is produced by Hartmann's boundary layers. On the contrary, Shercliff layers (boundary layers parallel to the field) produce recirculation allowing inertial effects to penetrate the heart of the flow, thus modifying the average velocity profile when the Reynolds number Re is sufficiently large. Similarly, Potherat, Sommeria & Moreau (2000) analytically predicted two typical phenomena likely to occur in such electromagnetically driven flows in annular geometry: first, a secondary recirculation related to inertial effects in the Hartmann boundary layer, and second, the possibility of a transverse dependence of the velocity in the bulk flow. These predictions were confirmed experimentally by the same authors. It is now well accepted that the main action of the magnetic field is thus to reduce the velocity gradients in its direction, and that the nature of the transition between strongly magnetized bidimensional flows and three-dimensional (3-D) flows is intimately linked to recirculations (Sommeria & Moreau 1982; Potherat 2012). Due to the substantial number of control parameters, there are still several unanswered questions regarding the different flow regimes observed in electrically driven annular duct flow.

More recently, several studies have focused on the destabilization of such flows for moderate Reynolds numbers, when the Hartmann layers become unstable. The experimental study by Moresco & Alboussière (2004a) looked at the distribution of currents in the flow and reported how the destabilization of Hartmann's boundary layers is controlled by the parameter $Re_H = Re/Ha$ which is a critical Reynolds number based on the thickness of the laminar Hartmann layer, with Ha the Hartmann number. In this experience, the transition to turbulence is observed for values of Re_H two orders of magnitude smaller than what is predicted by linear stability theory, thus suggesting the existence of a subcritical transition in this type of flow. These results have been completed by direct numerical simulations (Krasnov *et al.* 2004), proposing an explanation for this difference between simulations and experiments based on the growth of disturbances of finite amplitude near the boundary layers. In some cases it has been shown that the instability of the flow is rather controlled by the Reynolds number based on the thickness of the Shercliff layer (Potherat 2007). Moreover, it has also been shown numerically that current-driven flows in annular geometry can also become unstable at moderate Hartmann numbers, via centrifugal-type instability (Zhao, Zikanov & Krasnov 2011, 2012)

Such destabilization is also reported in other laboratory experiments. In Tabeling & Chabrierie (1981), it was shown that electrically driven flows can undergo a sequence of instabilities involving slow oscillations just before the transition to turbulence. In tall cylindrical apparatus, Boisson *et al.* (2012) and Boisson, Monchaux & Aumaitre (2017) have shown that travelling waves can appear when the forcing is large enough due to inertial terms. More recently, a Kelvin–Helmholtz destabilization of free shear layers generated near the electrodes has also been observed (Stelzer *et al.* 2015a,b). Finally, note that Messadek & Moreau (2002) also found that at very large Reynolds and Hartmann numbers, in a configuration involving a sheared layer, the flow exhibits quasi-2-D turbulence.

Most of the laboratory experiments described above rely on the generation of large forcing by the use of very strong magnetic field. For example, the experiences of Messadek

& Moreau (2002) reach $IB \sim 300$ AT (where I is the injected current and B is the magnetic field) in order to obtain high Reynolds number regimes. However, this is achieved by using magnetic fields relatively large (between 1 and 10 Tesla). Thus, these laboratory experiments describe inertial regimes, but always in a strongly magnetized limit, for which the interaction parameter N_I (table 2) is large. One of the motivations of the experiment reported here is to go beyond the classical inertial regime and to reach a fully turbulent state at small N_I . As shown in the next sections, this is made possible by three important features of the KEPLER experiment: a particularly thin-disc geometry (compared with the usual square section), a driving which mostly relies on a very large current (rather than strong magnetic field) and a large horizontal size leading to large Reynolds numbers.

Finally, the study of the fully turbulent flow of a magnetohydrodynamic thin disc finds direct application in astrophysics. For example, accretion discs, one of the most studied problems in astrophysical fluid dynamics, involve turbulent flows in which a fluid is in Keplerian rotation around a massive central body, usually a star, a protostar or a black hole. The exact mechanisms by which the angular momentum is transported outward in these discs remain unknown. Indeed, the enormous accretion rates observed by astrophysicists indicate that the transport of material inward, losing angular momentum, must be compensated by a large transport of angular momentum outward. Keplerian rotation profiles being hydrodynamically stable according to the Rayleigh criterion for centrifugal instability, a hydrodynamic linear instability cannot be invoked to explain this angular momentum transport (Rayleigh 1917; Ji *et al.* 2006; Velikhov *et al.* 2006; Fromang & Lesur 2019). In order to understand the existence of this regime, different mechanisms have been proposed like subcritical transition to turbulence (Lesur & Longaretti 2005), extraction of angular momentum by MHD winds from the disc (Lesur 2021), or the role of density stratification (Dubrulle *et al.* 2005). But the most accepted scenario is the magnetorotational instability (MRI) (Balbus & Hawley 1991), which explains how a conducting fluid in differential rotation subjected to a sufficiently large magnetic field can be destabilized towards a fully turbulent state. Although extensively studied numerically and theoretically, the experimental observation of MRI remains a major challenge for modern fluid dynamics (Sisan *et al.* 2004; Stefani *et al.* 2006; Roach *et al.* 2012), mainly due to the difficulty in achieving a high magnetic Reynolds number in the laboratory, but also because of the difficulty in generating a stable Keplerian flow. In this regard, it has been proposed that electrically conducting boundaries (Winarto *et al.* 2020) and electromagnetically driven flows might be an efficient configuration for stabilizing Rayleigh-unstable flows near the boundaries (Stefani & Gerbeth 2004) and satisfy the required conditions for observing MRI instability in the laboratory (Khalzov, Smolyakov & Ilgisonis 2010). The interest of our experiment with respect to this problem is therefore twofold: first, it reproduces the thin-disc configuration, the flow configuration and the presence of a magnetic field typical of astrophysical discs, but it also elucidates the regime of electromagnetically driven flows at large Reynolds number.

2. Experimental set-up

2.1. General description

The KEPLER experiment (see figure 1) consists of an annular cylindrical channel with an internal diameter $2R_i = 12$ cm and an external cylinder diameter $2R_o = 38$ cm (mean radius $r_m = 12.5$ cm, gap $\Delta r = 13$ cm). It is filled with Galinstan, a eutectic alloy of gallium, indium and tin, that is liquid at room temperature and whose physical characteristics are summarized in table 1. A strong electrical current (up to 3000 A) is

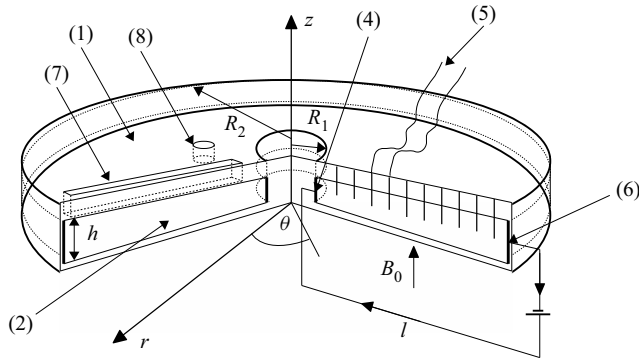


Figure 1. Sketch of the experimental set-up. A thin disc of diameter $D = 38$ cm and thickness $h = 1.5$ cm is filled with a liquid metal (Galinstan) and placed between two Helmholtz coils generating a vertical homogeneous magnetic field. The cell is confined by top and bottom walls (1) made of electrically insulating Plexiglas and by electrically conducting cylindrical walls acting as an anode (4) and cathode (6). The cross-section of the duct is rectangular (2), and characterized by a large aspect ratio $\Delta r/h \simeq 9$. The flow is entirely driven by the Lorentz force generated by the combined action of the vertical magnetic field (B_0) and the strong radial current (I) passing from the anode to the cathode. Velocity measurements are made by potential probes inserted in the top wall up to the middle of the gap (5) thanks to Doppler probes inserted in a rail inclined at an angle of 45° analogous to (7) not represented here for clarity. Induced magnetic field measurements were done thanks to Hall probes inserted in a rail (7) and the pressure sensor was inserted in the top wall (8).

Name	Galinstan MCP11
Chemical composition	68.5 % Ga, 21.5 % In, 10 % Sn
Density	$6.44 \times 10^3 \text{ kg m}^{-3}$ (293 K)
Electric conductivity	$3.46 \times 10^6 \text{ S m}^{-1}$
Melting point	254 K
Kinematic viscosity	$3.7 \times 10^{-7} \text{ m}^2 \text{ s}^{-1}$
Sound speed	2730 m s ⁻¹

Table 1. Physical properties of the liquid metal Galinstan used in the experiment.

injected radially by a direct current generator Power TEN P66 Series 53000 from the inner cylinder to the outer rim. The temperature of the inner cylinder is controlled by a water cooling system. Both electrodes are made of brass and protected from the Galinstan by an electrochemical deposit of nickel, in order to ensure a good electric contact with the liquid metal. The height of the cell is $h = 1.5$ cm, corresponding to a relatively large aspect ratio $\Gamma = \Delta r/h = 8.7$. The top and bottom walls are electrically insulating Plexiglas plates. The cylinder is placed between two large Helmholtz coils generating a homogeneous vertical magnetic field along the vertical z -axis. The coils are powered by two direct current generators, Ametek RS 20V-250A, producing magnetic fields of up to 110 mT. The combination of the radial current and the vertical magnetic field generates a strong Lorentz force in the azimuthal direction.

2.2. Measurement methods

The velocity field is recorded using two different measurement techniques. First, velocity profiles are measured with ultrasonic Doppler velocimetry, by using the commercial

Re	$U r_m / \nu$	$> 10^5$
Re_h	$U h / \nu$	$> 10^4$
Ha	$B_0 h (\sigma / \rho \nu)^{1/2}$	< 60 ($\sim 0.57 B_0$ [mT])
Rm	$U r_m / \eta$	$\ll 1$
Pm	$Rm / Re = \nu / \eta$	$\ll 1$
Υ	$I_0 / 2 \pi r_m h \sigma U B_0$	j_0 / j_{ind}
Re_H	$U \delta_{Ha} / \nu$	Re / Ha
Re_B	$U \delta_\Omega / \nu$	$Re^{1/2}$
Λ	$\sigma B_0^2 / \rho \Omega$	$\delta_\Omega^2 / \delta_{Ha}^2$
N_i	$\sigma B_0^2 h / \rho U (\Delta r / h)^2$	$Ha^2 / Re (\Delta r / h)^3 \sim 10 \Lambda$
δ_Ω	$\sqrt{\nu / \Omega}$	$\sim r_m / Re^{1/2}$
δ_{Ha}	$\sqrt{\rho \nu / \sigma B_0^2}$	$\sim h / Ha$

Table 2. List of dimensionless numbers.

system DOP3010 from Signal Processing SA, in which probes send ultrasonic pulses at regular intervals. The phase shift between the sent pulse and its echo on particles in the bulk (mostly oxides in liquid metals) is computed in order to obtain the velocity profile along the direction pointed by the Doppler probe. The Doppler probes are installed into the Plexiglas plates at an angle of 45° with the flow. Plexiglas and Galinstan have a close acoustic impedance, ensuring a good transmission of the ultrasonic pulses. Note that due to the angle, the measured velocity is a linear combination of the local azimuthal component of the velocity u_θ and the vertical component u_z .

In addition, both azimuthal and radial components of the velocity are also measured using potential probes. For a conductive fluid in motion, Ohm's law specifies that the current density $\mathbf{j} = \nabla \times \mathbf{B} / \mu_0$ is given by the relation $\mathbf{j} = -\sigma \nabla \phi + \sigma (\mathbf{u} \times \mathbf{B})$, where μ_0 is the vacuum magnetic permeability, σ is the electrical conductivity and ϕ is the electric potential. After having removed the injected current, the local velocity is deduced from the potential difference ($\delta\phi$) between two probes separated by a small distance d using the relation $U_\theta = \delta\phi / (B_0 d)$ where B_0 is the magnitude of the vertical magnetic field. Nine small electrodes (1 mm diameter, separated from each other by $d = 8$ mm) are inserted equidistantly into the top plate through holes located between inner and outer cylinders. These probes are nickel wires electrically insulated everywhere but at the tip. The mean component of the velocity is obtained through measurement of the voltage by a nanovoltmeter, Keithley Model 182, and filtered via a filter amplifier, Stanford Research Systems Model SR560 in DC mode. The turbulent fluctuations are obtained from amplification of the signal through a filter amplifier, Princeton Applied Research Low Noise Amplifier Model 1900, using smaller potential probes ($d = 4$ mm).

Pressure fluctuations are measured by a pressure sensor Kistler Type701A (sensitivity of $82.24 \text{ pC bar}^{-1}$, acquisition frequency 10 kHz), placed in contact with the liquid metal through a hole in the top Plexiglas plate and coupled to a charge amplifier Kistler Type5018. Finally, induced magnetic field were measured by a Teslameter F.W. Bell Model7030 connected to Hall probes (precision up to $\sim 10 \text{ } \mu\text{T}$) inserted in vertical holes in the Plexiglas plate around two millimetres away from the liquid metal.

3. Length scales and dimensionless numbers of the experiment

The dynamics of an incompressible electrically conducting fluid is described by the MHD equations, which couple the Navier–Stokes equation to the induction equation. The latter is

obtained from a combination of Maxwell's equations and Ohm's law, such that the system of equations is

$$\rho \frac{\partial \mathbf{u}}{\partial t} + \rho \mathbf{u} \cdot \nabla \mathbf{u} = -\nabla p + \rho \nu \Delta \mathbf{u} + \mathbf{j} \times \mathbf{B}, \quad (3.1)$$

$$\frac{\partial \mathbf{B}}{\partial t} = \nabla \times (\mathbf{u} \times \mathbf{B}) + \eta \Delta \mathbf{B}, \quad (3.2)$$

$$\nabla \cdot \mathbf{u} = 0 \quad \nabla \cdot \mathbf{B} = 0, \quad (3.3)$$

where \mathbf{u} is the velocity field, \mathbf{B} the magnetic field, \mathbf{j} the current density, ρ the liquid metal density, ν is the kinematic viscosity and $\eta = 1/(\mu_0\sigma)$ is the magnetic diffusivity (where μ_0 is the magnetic permeability and σ is the electrical conductivity) (table 1).

In addition to the physical properties of the fluid (ρ , ν , σ , μ_0) and the geometrical parameters of the experiment (h , r_m , Δr), the typical azimuthal velocity U of the fluid is controlled by the applied current I_0 and magnetic field B_0 . Our experiment is therefore described by a set of six independent dimensionless numbers, the two geometrical numbers $\Gamma = \Delta r/h$, h/r_m and the kinetic Reynolds number Re and Ha (table 2)

$$Re = \frac{Ur_m}{\nu} \quad \text{and} \quad Ha = B_0 h \left(\frac{\sigma}{\rho \nu} \right)^{1/2}. \quad (3.4a,b)$$

The Reynolds number compares advection with diffusion and the Hartmann number is a dimensionless measure of the Lorentz force (compared with viscous dissipation). Note that an important characteristic of the KEPLER experiment is the use of very high current $I_0 \sim 3000$ A, which leads to large Reynolds number ($Re > 10^5$) while the Hartmann number remains moderate ($Ha < 60$). In KEPLER experiment, $Ha \sim 0.57B_0$ with B_0 in mT. As discussed later, when the flow becomes quasi-bidimensional, a better definition of the Reynolds number is $Re_h = Uh/\nu$.

One can also define a magnetic Reynolds number $Rm = Ur_m/\eta$, which compares induction with magnetic diffusion in the induction equation. Alternatively, the magnetic Prandtl number $Pm = \nu/\eta$ can be used instead of Rm . In liquid metals, the kinematic viscosity is much smaller than the magnetic resistivity ($Pm = Rm/Re < 10^{-5}$). It follows that the characteristic time of the fluctuations of the magnetic field $\tau_b \sim l^2/\eta$ is far smaller than $\tau_v \sim l^2/\nu$ (i.e. $\tau_b/\tau_v \ll 1$). Therefore, in the limit of small induction ($Rm \ll 1$), \mathbf{b} follows \mathbf{u} in a 'quasi-static' way and the induction equation becomes (Moffatt 1961)

$$0 \simeq \mathbf{B}_0 \cdot \nabla \mathbf{u} + \eta \Delta \mathbf{b}. \quad (3.5)$$

Because our experiment operates hardly outside this regime ($Rm = 1$ at most), MHD phenomena requiring large induction effects are not expected. This rules out the possibility of observing dynamo action or MRI instability for instance.

The dimensionless current is defined as

$$\gamma = \frac{I_0}{2\pi r_m h \sigma U B_0}. \quad (3.6)$$

It is the ratio between the current density $j_0 = I_0/2\pi rh$ directly injected between the radial electrodes and the current $j_{ind} \simeq \sigma u_\theta B_0$ induced in the radial direction by the motion of the fluid (at lowest order). Since this induced current is mostly generated in the bulk flow, it controls the distribution of the current: at low γ , most of the current passes through the top and bottom boundary layers, while it occupies the whole height of the cell at $\gamma \gg 1$.

In principle, these six dimensionless numbers are sufficient to fully describe the flow. However, it is useful to define two additional dimensionless ratios. The first one is related to the boundary layers generated at the vertical walls of the experiment: two different types of boundary layers can be generated in such MHD rotating flows at the top and bottom boundaries. First, Hartmann layers arise when a shear flow approaches walls perpendicular to a magnetic field. These boundary layers are characterized by a force balance between the Lorentz force and the viscous dissipation inside a typical thickness δ_{Ha} given by $\delta_{Ha}^{-1} \sim B\sqrt{\sigma/\rho\nu}$. These layers are known (Murgatroyd 1953; Moresco & Albuossière 2004a) to become unstable when the Reynolds number of the boundary layer $Re_H = U\delta_{Ha}/\nu = Re/Ha$ becomes sufficiently large. On the other hand, purely hydrodynamical boundary layers can also be generated at the Hartmann walls: as the rapidly rotating fluid reaches the boundaries where viscous forces dominate, an imbalance between the decreasing centrifugal force and the radial pressure gradient produces a radial flow in a boundary layer of typical thickness $\delta_\Omega = (\nu/\Omega)^{1/2}$. Such Bödewadt layers can also exhibit an instability at large Reynolds number. Following Davidson & Potherat (2002), we introduce the Elsasser number defined by

$$\Lambda = \frac{\sigma B_0^2}{\rho\Omega} = \frac{\delta_\Omega^2}{\delta_{Ha}^2}. \quad (3.7)$$

As a ratio between the Lorentz and centrifugal forces, the Elsasser number tells which effect dominates the establishment of the boundary layer close to the walls.

One last important dimensionless number is the interaction parameter (also known as the Stuart number) which is the ratio between the Lorentz force and inertia, up to some geometric factor

$$N_t = \frac{\sigma B_0^2 h}{\rho U} \left(\frac{\Delta r}{h}\right)^2 = \frac{Ha^2}{Re} \left(\frac{\Delta r}{h}\right)^3, \quad (3.8)$$

where N_t quantifies the strength of the magnetic field compared with the inertia of the flow. It has been shown that this true interaction parameter accurately describes the dimensionality of MHD flows (Sommeria & Moreau 1982; Messadek & Moreau 2002; Potherat & Klein 2014). As N_t becomes large, the velocity field becomes independent of the direction in which the magnetic field is applied. In particular, if both Re and N_t are sufficiently large, a quasi-bidimensional turbulent flow is expected.

3.1. Parameter space and outline of the results

Figure 2 summarizes the various results obtained with the KEPLER experiment. The colour plot shows interpolated values of $\log(u_\theta)$ in the (I_0, B_0) parameter space. Four different domains have been identified. These regimes will be described in more details in the next sections, but it is insightful to give a short overview of the parameter space now: at large magnetic field ($N_t > 10$, indicated by the red dashed line) and small Reynolds number ($Re < 9000$, indicated by the black solid line), the viscous–ideal regime corresponds to a balance between the Lorentz force and the viscous dissipation, and is characterized by a strong value of the external magnetic field such that the induction term $\mathbf{u} \times \mathbf{B}_0$ dominates the magnetic diffusion term $\eta\Delta\mathbf{b}$ where \mathbf{b} is the induced field. The flow is laminar, and the velocity field scales as $u_\theta \propto I_0/r$, independently of B .

At smaller magnetic field but moderate Reynolds number, the inertial–resistive regime is obtained. The Lorentz force is now balanced by inertia, but the boundary layers remain laminar. In addition, a significant amount of current passes through the bulk flow.

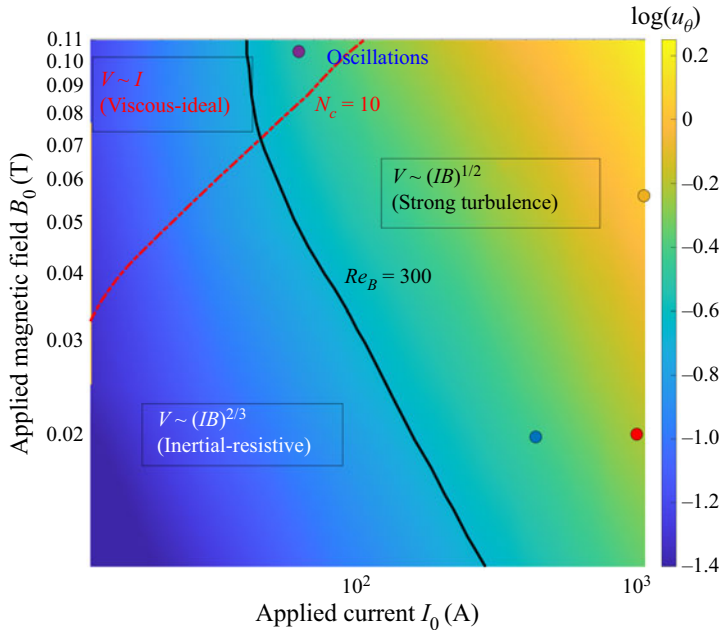


Figure 2. Map of the logarithm of the mean azimuthal flow, $\log(\bar{u}_\theta)$ as a function of (I_0, B_0) , measured with the potential probes. The red dashed line ($N_c = 10$) and the black solid line ($Re_B = 300$) delimitate the transition between the different regimes in the experiment. The points indicate the four typical runs discussed in § 6.

The corresponding velocity field scales as $u_\theta \propto (IB)^{2/3} r^{-1/3} f(\Delta r/r)$ (f being an unknown function) and remains in a quasi-Keplerian state. Note that the first regime has been identified in previous MHD experiments and well described theoretically (Baylis 1971; Messadek & Moreau 2002). Although not discussed in detail by previous experimental studies, analysis of published data suggests that the second regime has also been observed in previous experiments.

However, when the Reynolds number is increased, the flow then bifurcates to a quasi-bidimensional turbulent flow regime, in which both the bulk and the boundary layers are turbulent. In this so-called ultimate regime, we observe a new scaling $u_\theta \propto \sqrt{IB}/r$, corresponding to a turbulent Keplerian velocity profile sharing some similarities with the velocity profile expected in accretion discs. This turbulent regime is observed only if the magnetic field is not too large, for $N_t < 10$, and therefore requires an extremely large applied current.

Finally, at large magnetic field ($N_t > 10$) and large Reynolds number ($Re > 9000$), we observe a bi-dimensional turbulent regime which exhibits a slow dynamics and condensation of the energy at large scale.

4. Flow regimes and transition to turbulence

Most of previous experimental studies focused either on the laminar regime (obtained at small Re , large Ha) or on the regime of quasi-bidimensional turbulence (observed at large N_t , large Re). The novelty of the KEPLER experiment lies in the use of very large applied current (maximum current $I_0^m = 3000$ A) and a moderate applied magnetic field (maximum field $B_0^m \sim 0.11$ T). The forcing, controlled by the product $I_0 B_0$, can therefore

reach very large values ($I_0^m B_0^m \sim 300$ TA) while keeping the Hartmann number small ($Ha = 60$ at most). By comparison, Messadek & Moreau (2002) reach comparable values, $I_0^m B_0^m \sim 500$ TA, but only at very large magnetic fields ($B_0 \sim 5$ T), corresponding to $Ha \sim 1500$. Here, the smallness of Ha makes possible to observe a full destabilization of the Hartmann layers, leading to flows that are significantly more turbulent. On the other hand, the relatively weak values of our applied magnetic fields are somehow compensated by the large aspect ratio of the experiment $\Delta r/h \sim 9$ and the large value of Δr . This leads to values of the interaction parameter N_t that are not too small, allowing us to observe quasi-bidimensional turbulence in some parameter range.

To see how these different regimes are generated, figure 3(a) shows time-averaged measurements obtained from the potential probes located at a radial distance $r = 12$ cm, approximately in the middle of the cylindrical gap. We plot the mean value of u_θ as a function of the applied current I_0 , for different values of the magnetic field, ranging from $B_0 = 6$ mT to the highest possible value $B_0 = 110$ mT. The typical velocities of the flow span a large range of values, from 1 cm s^{-1} to a few metres per second, yielding $Re \sim 10^5$ at most. Since the applied field can both drive flow motions and laminarize it, figure 3 shows the same data but with u_θ plotted as a function of $I_0 B_0$ instead. Three different scaling laws can be deduced from these data.

4.1. Viscous–ideal flows

At large magnetic field ($Ha \geq 30$), figure 3(a) shows that the velocity scales linearly with the applied current at low I_0 . This regime has been first described theoretically by Baylis & Hunt (1971) for a laminar axisymmetric flow in a toroidal channel of square cross-section, and later confirmed by most experimental studies mentioned in the introduction.

The theoretical prediction for this laminar flow can be retrieved by simple arguments. When the Elsasser number Λ is sufficiently large, the Hartmann layers are much thinner than Bödewadt layers, meaning that most of the velocity gradient occurs in layers of size δ_{Ha} . In addition, if Υ is small, most of the applied current I_0 passes through the two Hartmann layers with a current density $\mathbf{j} \simeq (I_0/(2\pi r(2\delta_{Ha})))\mathbf{e}_r$ in each layer. The azimuthal Lorentz force $F_\theta = j_r B_0$ is then balanced in the Hartmann layer by the viscous dissipation $\rho\nu\Delta\mathbf{u} \sim \rho\nu u_\theta/\delta_{Ha}^2\mathbf{e}_\theta$, leading to

$$U_\theta = \frac{I_0}{4\pi r\sqrt{\rho\nu\sigma}}. \tag{4.1}$$

In this expression, B_0 does not appear explicitly, although it controls the bi-dimensionalization of the flow. Note that this expression stands only if the Shercliff boundary layers generated at the surface of the cylinders parallel to the magnetic field do not interfere with the bulk flow. This means $r_2 - r_1 \gg h/\sqrt{Ha}$, which is well satisfied in the KEPLER experiment. Note that the ideal term used here refers to the fact that magnetic diffusion term $\eta\Delta\mathbf{b}$ can be neglected compared with the induction $\mathbf{u}B_0$. It is, however, important to mention that this comes from the fact that the field B_0 is strong, and is quite different from the classical ideal MHD generally obtained when $Rm \gg 1$.

The velocity field obtained at large B_0 and low current agrees very well with this prediction, indicated by the dashed line in figure 3.

4.2. Inertial–resistive flows

Figure 3(b) shows that, in fact, two different scaling laws can be obtained at low forcing: for $Ha \geq 30$, the linear scaling $u_\theta \propto I_0$ of the viscous–ideal regime described above,

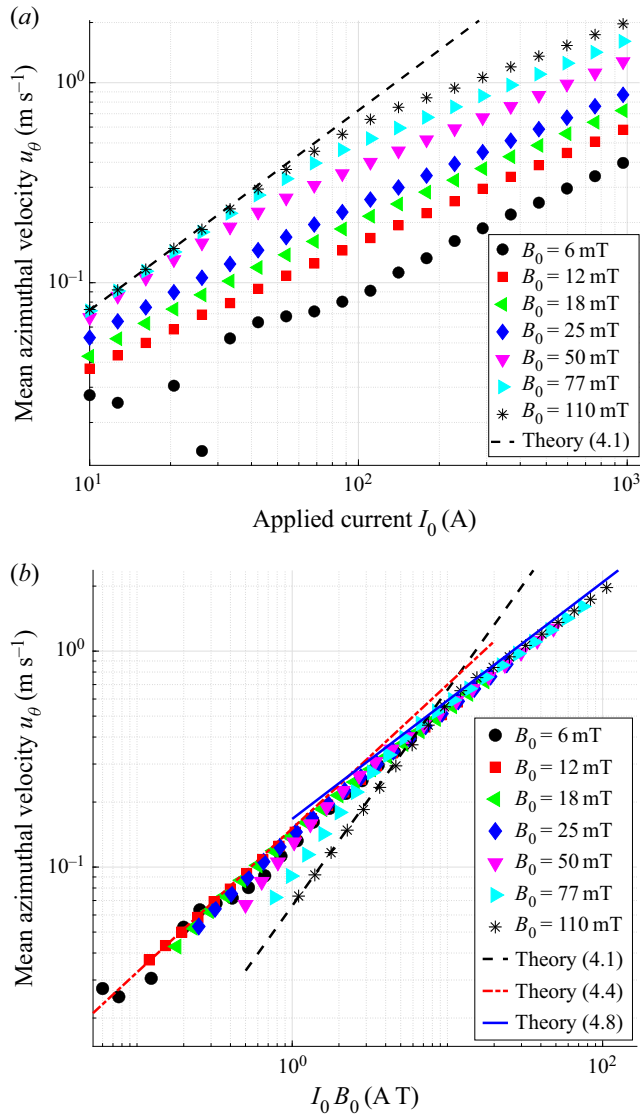


Figure 3. (a) Mean azimuthal flow \bar{u}_θ vs the applied current product I_0 measured by the potential probes for different values of the applied field B_0 . The velocity is measured at a radial distance from the centre $r = 12$ cm. (b) Same, plotted as a function of the product $I_0 B_0$. Three different scaling laws can be observed, indicated by the solid line ($u_\theta \propto \sqrt{I_0 B_0}$), the dashed line ($u_\theta \propto I_0$) and the dash-dotted line ($u_\theta \propto (I_0 B_0)^{2/3}$). Here, $Ha \sim 0.57 B_0$ with B_0 in mT.

and a scaling of the form $u_\theta \propto (I_0 B_0)^{2/3}$ at smaller Ha . A similar regime seems to have been observed in at least one previous experiments (Baylis 1971) and one recent numerical study (Poye *et al.* 2020). As shown by figure 3, this regime is observed for $I_0 B_0 < 10$ and $B_0 < 40$ mT. We give below simple arguments to explain this regime, following closely Poye *et al.* (2020).

In the bulk flow, inertia terms in the azimuthal direction are balanced by the applied Lorentz force $I_0 B_0 / (2\pi r h)$. In contrast to the previous case, experimental values of \mathcal{T} suggest that the fraction of current passing through the bulk should be relatively large.

It follows that

$$u_\theta \simeq \frac{I_0 B_0}{2\pi \rho h u_r} f\left(\frac{\Delta r}{r}\right), \quad (4.2)$$

where the inertial term $\rho u_r u_\theta / r$ is larger than $\rho u_r \partial_r u_\theta$ because r is smaller than the gap Δr in the inner part of the disc. At large radii, $r > \Delta r$ and the second term might be dominant, which is taken into account by the function f . Because $r \sim \Delta r$ in any cases, the function f is expected to be of order one and the choice of the inertial term will not change the scaling law.

For moderate magnetic fields, when $\Lambda \leq 1$, the radial inflow near the boundaries is mostly dominated by the Bödewadt layers. The corresponding imbalance between the centrifugal force in the layer and the pressure gradient $\partial_r p \sim \rho u_\theta^2$ leads to

$$u_r^{BL} \sim \frac{\delta_B^2 u_\theta^2}{\nu r}, \quad (4.3)$$

where u_r^{BL} is the typical radial velocity in the Bödewadt layer of thickness δ_B . Because u_z is presumably small in the bulk flow, incompressibility implies $\int_0^h u_r dr \approx 0$ at lowest order and so $u_r h \sim 2\delta_B u_r^{BL}$. By combining this last result, with expressions (4.2) and (4.3), one finally obtains

$$u_\theta = \left(\frac{I_0 B_0}{4\pi \rho \sqrt{\nu}}\right)^{2/3} r^{-1/3} f\left(\frac{\Delta r}{r}\right). \quad (4.4)$$

Note that the unknown function f may influence the radial dependence, but not the scaling law for the magnitude of the flow because $f \sim 1$. Although the scaling law (4.4) shares some similarities with the one found by Poye *et al.* (2020), our full expression is quite different, and leads to values one order of magnitude smaller. This is due to some differences between our experiment and the set-up studied by these authors, in particular the relatively large aspect ratio used here ($\Delta r/h \sim 9$) and the fact that $r_m \sim \Delta r$ in the KEPLER experiment. When plotting the results of Baylis (1971) in this form, it appears that their data follow a similar dependence $u_\theta \propto (I_0 B_0)^{2/3}$. A dependence $u_\theta \propto (I_0)^{2/3}$ based on a different argument was also observed by Potherat & Klein (2014), although their set-up is quite different. At the exception of Messadek & Moreau (2002) where a very turbulent flow is reached, we argue that this regime is probably the one mostly observed in previous experiments operating at large Reynolds number.

Prediction (4.4) (with $f = 1$) is shown by the dash-dotted line in figure 3. It fits our experimental data with a very good agreement.

4.3. Keplerian turbulence

Finally, when the forcing due to the Lorentz force becomes sufficiently strong, the flow undergoes a new transition from the previous laminar flows toward a presumably turbulent state. Figure 4(a) shows that for $I_0 B_0 > 10$, all the data collapse on a single curve. The best power law to fit the data is $u_\theta \propto (I_0 B_0)^{0.54 \pm 0.01}$.

This result can be understood by assuming that the bulk flow is fully turbulent, such that the Reynolds stress gradient $\rho \partial_i \bar{u}_i \bar{u}_j$ overcomes the inertial terms involving the mean velocity $\rho (\bar{u}_i \partial_i) \bar{u}_j$. In addition, because of the large aspect ratio of the experiment $h \ll r_m, \Delta r$, the Reynolds stress is mostly dominated by the components $\tau_{iz} = \rho \partial_z \bar{u}_i \bar{u}_z$.

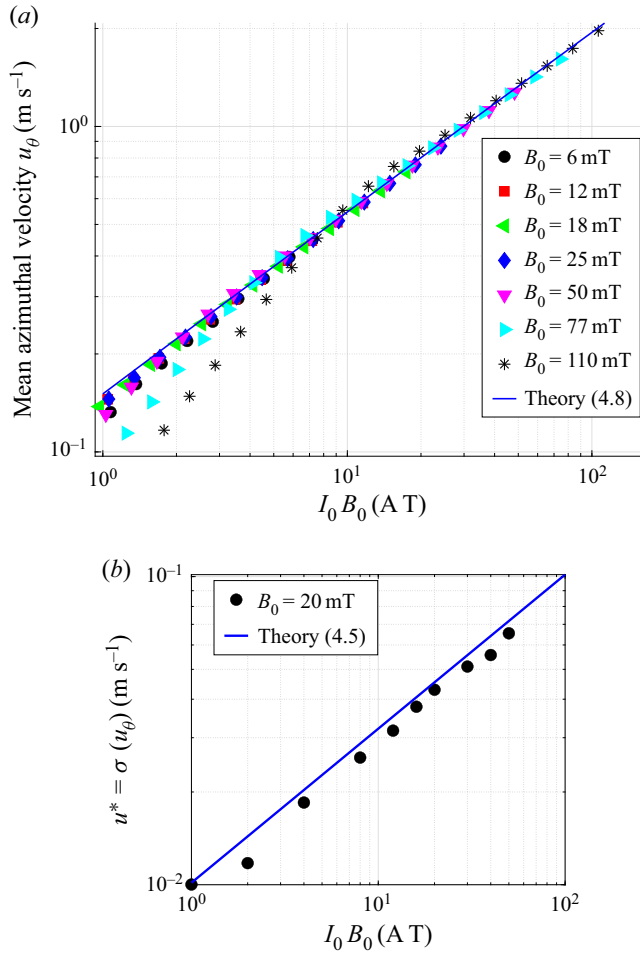


Figure 4. (a) Mean azimuthal flow u_θ vs the forcing $I_0 B_0$ in the fully turbulent regime. All our data collapse onto the theoretical prediction given by (4.8) (solid line). (b) Turbulent velocity u^* estimated from the standard deviation of u_θ for $B = 20$ mT, and compared with (4.5). Here, $Ha \sim 0.57B_0$ with B_0 in mT.

The azimuthal component of the Navier–Stokes equation therefore reduces to a balance between the Reynolds stress $\rho \partial_z \overline{u_\theta u_z}$ and the applied Lorentz force

$$u^* = \sqrt{\frac{I_0 B_0}{4\pi\rho r}}, \quad (4.5)$$

where the additional factor 2 comes from the estimate $\partial_z \overline{u_\theta u_z} \sim 2(u^*)^2/h$, with u^* the typical velocity of the turbulent structures. This prediction for the intensity of the turbulent fluctuations matches very well our experimental data, as shown by figure 4(b).

In the KEPLER experiment, the relevant boundary layers at the vertical wall are either the Hartmann layer at high Λ or the Bödewadt layer at low Λ . In the former, the stability of the layer is controlled by the Reynolds number Re_H based on δ_H , while in the latter, the relevant critical number is the Reynolds number Re_B based on the thickness of the Bödewadt layer. Moresco & Alboussière (2004b) have predicted that pure Hartmann layers should become turbulent for $Re_H = Ha/Re > 400$. Although it is well known that

this criterion strongly depends on the Elsasser number when rotation effects are present (Davidson & Potherat 2002; Moresco & Alboussière 2004b), we expect a similar value here, since Λ is never much larger than one in our experiment (except in the viscous–ideal regime where $\Lambda \sim 10$). In the regime studied here, as long as the forcing $I_0 B_0$ remains larger than 10, Re_H is between 400 and 2500 and R_B is larger than 200. It is therefore reasonable to expect the Hartmann–Bödewadt boundary layers to become turbulent at large forcing. Let assume a classical logarithmic profile for the turbulent boundary layer

$$\frac{\bar{u}_\theta(z)}{u^*} = \frac{1}{\kappa} \ln\left(\frac{u^* z}{\nu}\right) + C, \quad (4.6)$$

where κ is the Kármán constant and $C \approx 5$. Figure 4 shows that the turbulence intensity is relatively small, $u^*/\bar{u}_\theta \sim 3.10^{-2} \ll 1$, so (4.6) evaluated in the bulk ($z = h/2$) can be approximated by

$$\frac{\bar{u}_\theta}{u^*} = \frac{\ln(Re_h)}{\kappa}, \quad (4.7)$$

where the Reynolds number is supposed large enough to overcome contributions from neglected terms. By combining relations (4.5) and (4.7), we finally obtain the following prediction for the turbulent regime:

$$\bar{u}_\theta = \alpha \frac{\ln Re_h}{\kappa} \sqrt{\frac{I_0 B_0}{4\pi\rho r}}. \quad (4.8)$$

Note that because of the assumptions made during the derivation of this law, agreement between this prediction and experiments is only expected up to some pre-factor α of order one. In particular, MHD effects may very well modify the properties of the turbulent layer through the value of the parameters κ and C .

Despite these approximations, solution (4.8) with $\alpha = 1.5$, represented by the solid blue line in figure 4, matches remarkably well the experimental data. In particular, figure 4 shows that the logarithmic correction is necessary to fit the data, as it clearly increases the exponent of the power law.

Several remarks can be made on this prediction. First, except for the logarithmic correction, it is independent of h . This is reminiscent of the turbulent nature of the boundary layers. This expression is only valid in the limit of a thin-disc geometry, which leads to take h rather than r in the nonlinear term. When h is increased (experiments not reported here), we observed that this Keplerian profile (the radial scaling in $r^{-1/2}$) disappears. However, the square-root dependency in $I_0 B_0$ stands because it comes from a natural balance between the advection and the Lorentz force (Boisson *et al.* 2017). Note also that because this expression requires a destabilization of the boundary layers, it relies on a 3-D cascade of energy. This forward transfer of energy towards small scales is, however, only required for scales smaller than the typical thickness h , and no constrains exists on the larger scales. This explains why the scaling law (4.8) can be associated with quasi-bidimensional turbulence. On the other hand, this regime is only observed for interaction parameter not too large, namely $N_t < 10$. It means that although quasi-bidimensional, it cannot be described by purely 2-D Navier–Stokes equations.

Because the angular velocity profile is $\Omega \propto r^{-3/2}$, we refer to this solution as Keplerian turbulence. Although generated through a different mechanism, such profiles are expected in many astrophysical objects in which the centrifugal force balances gravity forces, as discussed in more details in § 5.

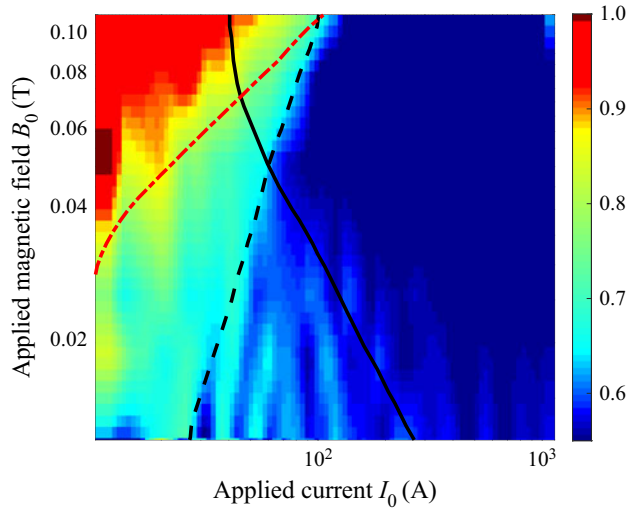


Figure 5. Colour map of the exponent ξ of the mean azimuthal flow $u_\theta \propto I_0^\xi$ in the parameter space (I_0, B_0) . The three regimes $\xi \sim 1$, $\xi \sim 2/3$ and $\xi \sim 1/2$ can be clearly distinguished (see the text).

4.4. Transitions between the different regimes

Figure 5 is very insightful to understand what controls the transition between the different regimes discussed above. To obtain this figure, we calculate the characteristic exponent of the scaling law

$$\xi = \frac{\partial \ln(\bar{u}_\theta)}{\partial \ln I_0} \quad (4.9)$$

and plot it in the parameter space (I_0, B_0) . The red area corresponds to the viscous–ideal regime ($\xi \sim 1$), the light blue to the inertial–resistive case ($\xi \sim 2/3$) and the dark blue to the Keplerian turbulence ($\xi \sim 1/2$). The red dash-dotted line corresponds to $N_t = 10$ and delimitates the region between strong and moderate magnetic field. Indeed, for large interaction parameter, most of the current passes through the thin Hartmann layers where the corresponding Lorentz force is balanced by viscosity (rather than inertia). As N_t is reduced below 10, the Bödewadt boundary layer generates a strong radial inflow near the wall. The interaction between this wind and the inertia in the bulk leads to the $2/3$ scaling law, as explained in the previous section. Note that in this regime, the Reynolds number Re is sufficiently small so the flow remains laminar. Alternatively, this transition can be predicted by balancing the two expressions for the mean azimuthal velocity given by (4.1) and (4.4), leading to the (velocity-free) dimensionless ratio $4\pi r^2 B_0^2 \sqrt{\nu \sigma^3} / I_0 \sqrt{\rho}$. The transition between the viscous–ideal and the inertial–resistive regime then occurs when this ratio is equal to one. Note that this ratio is an Elsasser number Λ in which the velocity is evaluated thanks to (4.1).

The transition from the $2/3$ regime to the turbulent one is less trivial. At small magnetic field, the Bödewadt layer is much smaller than the Hartmann one, and its stability is fully controlled by a critical Reynolds number $Re_B = u \delta_B / \nu$ based on the Bödewadt layer thickness (black solid line). In contrast, at large magnetic field, the stability of the thinner Hartmann layer is measured by the Reynolds number Re_H based on the thickness of this layer. We observe that the flow consequently bifurcates to the Keplerian turbulent regime along the line $Re_B \sim 400$ (solid black line) at low field, while the transition rather takes

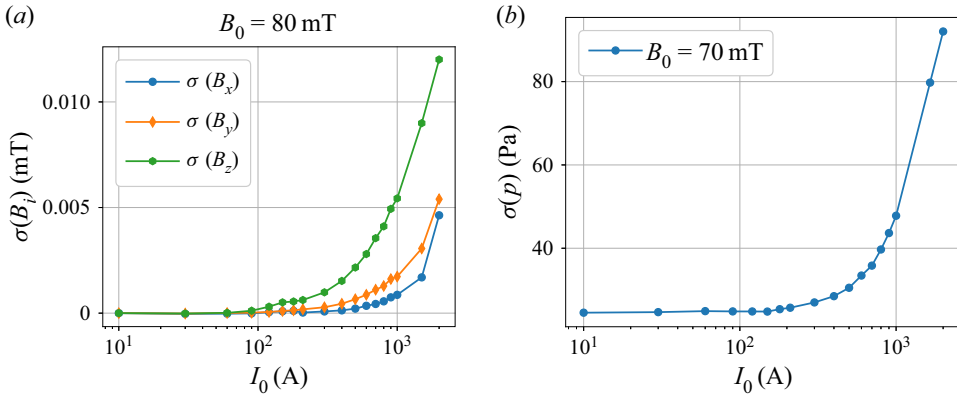


Figure 6. (a) Fluctuations (standard deviation) of the three components of the magnetic field as a function of the injected current I for an imposed magnetic field $B_0 = 800G$ (80 mT). (b) Fluctuations (standard deviation) of the pressure as a function of the injected current I for an imposed magnetic field $B_0 = 700G$ (70 mT).

place at a critical $Re_H \sim 300$ (dashed black line) at large field (for $B_0 > 50$ mT). Figure 5 therefore strongly suggests that the transition to the Keplerian turbulence is therefore ultimately triggered by the instability of Hartmann–Bödewadt layers.

Figures 6(a) and 6(b) show that the transition to turbulence in the experiment is associated with a strong (yet continuous) increase of the fluctuations of both induced magnetic field and pressure, without hysteresis. These results suggest that the Keplerian turbulence always occurs through a smooth supercritical transition.

4.5. Energy budget

Because conducting fluids can either dissipate energy viscously or by ohmic dissipation, the question of the energy budget of such electromagnetically driven flows is highly non-trivial. In electromagnetically driven flows, the energy equation is (Reddy, Fauve & Gissinger 2018)

$$\partial_t E_u = -D_v + T, \tag{4.10}$$

$$\partial_t E_b = -D_\eta - T + F, \tag{4.11}$$

where $E_u = \rho \int_V d^3x (\mathbf{u}^2/2)$, (respectively $E_b = \int_V d^3x (\mathbf{B}^2/2\mu_0)$) is the total kinetic (respectively magnetic) energy, $D_v = \rho\nu \int_V d^3x (\nabla \times \mathbf{u})^2$ (respectively $D_\eta = (1/\sigma) \int_V d^3x j^2$) is the viscous (respectively ohmic) dissipation; $T = (1/\mu_0) \int_V d^3x \mathbf{B} \otimes \mathbf{B} : \nabla \otimes \mathbf{u}$ is the term which couples the two equation and corresponds to the transfer of energy between the two fields and $F = \eta \oint_{\partial V} d\mathbf{S} \cdot (\mathbf{j} \times \mathbf{B})$ is the injected power.

In addition, one can also define the efficiency γ of the transformation as the ratio between the work of the Lorentz force and the total injected power $\gamma = T/F$. In stationary state, this measure of the amount of energy which is transferred to the kinetic part can also be written $\gamma = D_v/(D_v + D_\eta)$. This energy budget essentially depends on the flow regime, or more precisely on the degree of turbulence in the flow. First, in the viscous–ideal regime, the velocity gradients are essentially confined to the two top and bottom Hartmann boundary layers and the electrically current almost entirely passes through these layers. At the leading order, the current density is therefore given by $j \sim I_0/(4\pi r\delta_{Ha})$, and the

dissipations are given by

$$D_v \sim \frac{2\rho v S U^2}{\delta_{Ha}}, \tag{4.12}$$

$$D_\eta \sim \frac{2S I_0^2}{(4\pi r)^2 \delta_{Ha}}, \tag{4.13}$$

where S is the surface of the endcap. In the laminar regime, the velocity U is given by expression (4.1), and the dissipation ratio D_v/D_η is simply equal to one. The efficiency γ of the magnetic to kinetic energy conversion is therefore 50 %.

An exact calculation is not possible in the turbulent regime, but a general trend can be obtained: our scaling laws in this regime suggest that most of the viscous dissipation occurs in the Bodewadt boundary layer of typical size δ_Ω , and that the electrical current flows through the entire height of the channel. At leading order one would get $j \sim I_0/(2\pi rh)$ and

$$D_v \sim \frac{\rho v S U^2}{\delta_\Omega} \sim \frac{\rho v S U^{5/2}}{\sqrt{vr}}, \tag{4.14}$$

$$D_\eta \sim \frac{S I_0^2}{\sigma 4\pi^2 r^2 h}. \tag{4.15}$$

This leads to the dissipation ratio: $D_v/D_\eta \sim 4\pi^2 r^{3/2} v^{1/2} h \sigma (U^{5/2}/I_0^2)$ where the prefactor is equal to 0.1 in our set-up. By setting $U \sim 1 \text{ m s}^{-1}$ and $I_0 \sim 1000 \text{ A}$ as typical values of the turbulent regime, one gets $D_v/D_\eta \sim 10^{-7}$. In other words, the turbulence ‘destroys’ the efficiency of the energy transformation, and the dissipation in the turbulent regime is almost entirely due to ohmic dissipation, thus leading to a strong Joule heating of the liquid metal at large current and large magnetic field. As explained in § 2, the inner cylinder is therefore cooled in order to keep the experiment at variations of σ less than one per cent.

These results of an efficiency bounded by 50 % and decreasing with the level of turbulence are surprisingly similar to the one obtained by Reddy *et al.* (2018) in a very different MHD set-up, suggesting some universal behaviour of the energy budget of electromagnetically driven flows.

4.6. Low frequency oscillations

At large magnetic field and moderate current, there is a small region of the parameter space in which both Re_B and N_t are beyond their critical values Re_B^c and N_t^c . Interestingly, in this region, the velocity field exhibits a slow dynamics characterized by low frequency oscillations and interpreted as large scale structures being advected by the mean flow.

Indeed, for $B_0 > 95 \text{ mT}$, $30 \text{ A} < I_0 < 100 \text{ A}$, the frequency spectra generally show a peak of energy at low frequencies ($f \sim 1\text{--}5 \text{ Hz}$). Time series of figure 7(a) show that this condensate of energy at large scale corresponds to a periodic oscillation of the flow with its lowest frequency at $f \sim 2 \text{ Hz}$, quite comparable to the advection time $t_u = \Delta r/u_\theta \sim 5 \times 10^{-1} \text{ s}$. As shown by figure 7(b), these oscillations appear only at a critical current $I_0 \sim 30 \text{ A}$, corresponding to $Re_B > Re_B^c = 400$. The transition to this regime takes the form of a supercritical bifurcation which occurs only in a given range of current with no sign of hysteresis. As the current is increased at fixed magnetic field, the amplitude of these oscillations suddenly goes to zero (for $N_t \sim 10$) and they are replaced by the turbulent flow described above (see figure 7c).

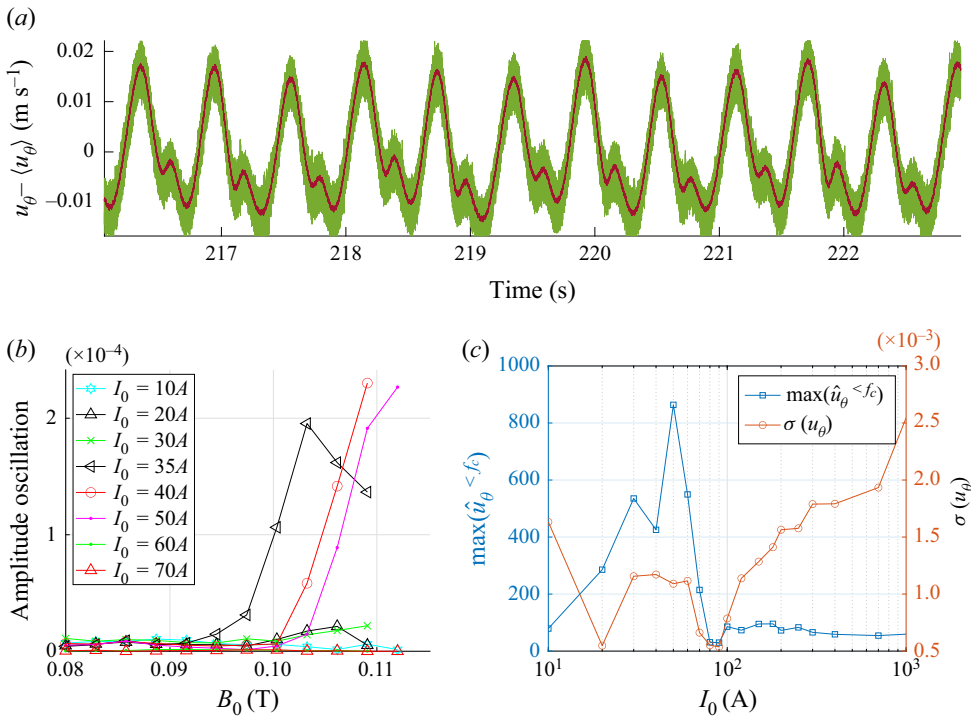


Figure 7. (a) Time series of the fluctuations of u_θ , measured with a potential probe for $B_0 = 110$ mT and $I = 30$ A. (b) Amplitude of the low frequency oscillation as a function of the magnetic field B_0 for different values of I_0 . (c) Same as a function of the current, together with the standard deviation of the azimuthal component of the velocity.

These results are very close to the ones obtained by Messadek & Moreau (2002), who reported similar low frequency oscillations. In their experiment, the current was injected by an array of electrodes located at an intermediate radius between the inner electrode and the outer cylinder of the experiment. These oscillations were therefore attributed to an instability of the shear layer generated near the electrodes between the active flow and the fluid at rest in the outer part of the experiment. There is, however, no steady region in our experiment, since the current is injected directly between the inner and the outer cylinder. These oscillations are more likely to be the consequence of some boundary layer instability. In this perspective, it is interesting to note that the Reynolds number based on the thickness of Shercliff layers generated at the radial boundaries is also relatively large ($Re_{sh} > 10^3$), such that an instability of these layers could be responsible for the oscillations. In this regard, these results are much closer to the periodic oscillations found by Tabeling near the onset of turbulence in electromagnetically driven Taylor–Couette flows (Tabeling & Chabrierie 1981).

In any case, these oscillations can be attributed to large scale bi-dimensional structures of typical size $l \sim 6$ cm which are advected by the mean azimuthal flow. Because they occur in the region delimited by ($N_t > 10, Re > 9000$), they could in principle be described by purely 2-D Navier–Stokes equations.

5. Velocity profiles and transport of angular momentum

Expressions (4.1), (4.4) and (4.8) lead to three different predictions for the velocity profile. Interestingly, each of these profiles describes a well-known physical situation encountered

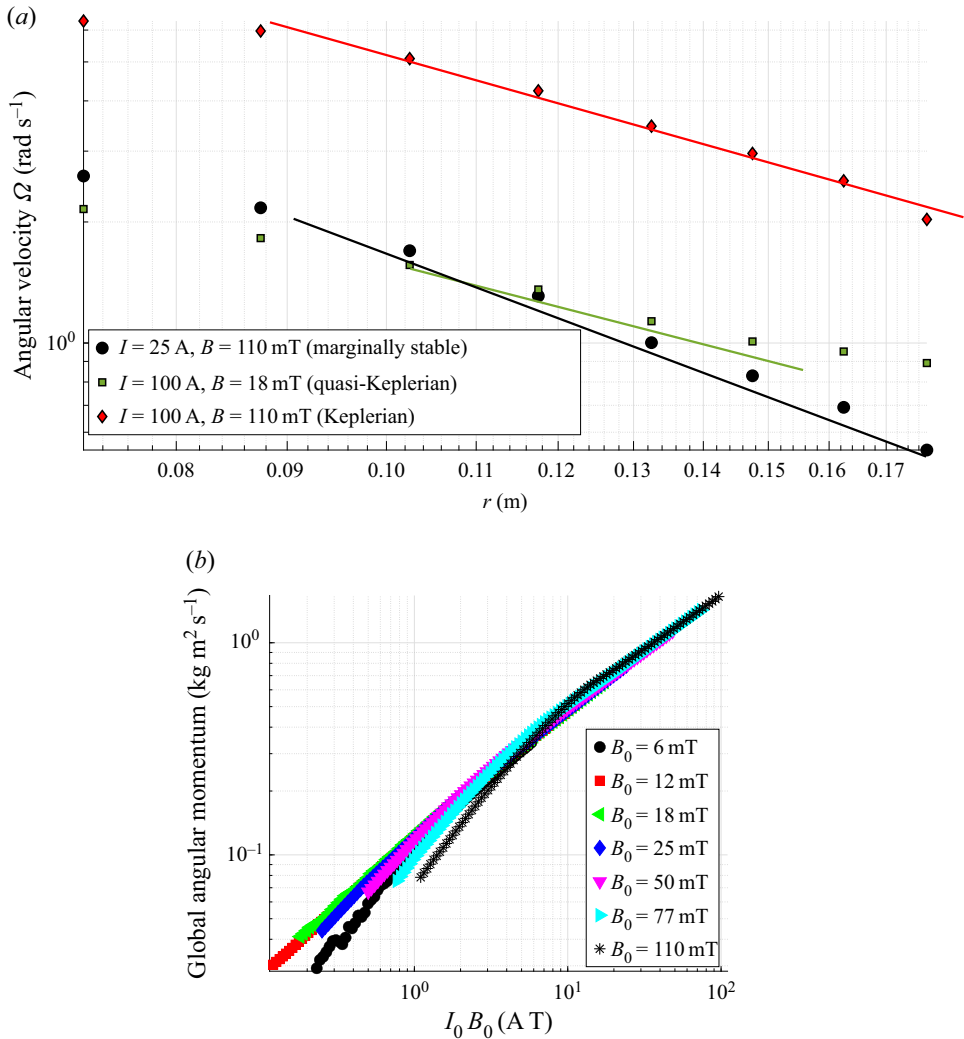


Figure 8. (a) Angular velocity $\Omega(r)$ obtained from potential probes, for three typical sets of parameters (I_0, B_0) , corresponding to the three different regimes predicted. (b) Global angular momentum vs $I_0 B_0$. Here, $Ha \sim 0.57B_0$ with B_0 in mT.

when studying the stability of toroidal flows. Figure 8(a) shows the angular velocity Ω for three different sets of parameters corresponding to these three regimes.

First, the black circles correspond to the viscous–ideal profile $\Omega \propto 1/r^2$ which generates an angular momentum $l = \Omega r^2$ that is constant in radius. This profile is therefore marginally stable, since $l = \text{cste}$ is precisely Rayleigh’s criterion for the stability of inviscid circular flows. Except close to the inner cylinder, the data are relatively close to the prediction. Note that the transport of angular momentum is then achieved by the viscous dissipation in the boundary layer.

The inertial–resistive regime (green squares) exhibits a less steep profile, as predicted by (4.4). This type of profile between global rotation and marginal stability (in which $q = -\partial \ln \Omega / \partial \ln r$ is between 0 and 2) is generally called a quasi-Keplerian profile. However, if the theory succeeds in predicting the magnitude of the flow, the predicted profile

$\Omega \propto r^{-4/3}$ is only observed for a small range of r in the middle of the gap. This is not surprising, as the unknown function $f(\Delta r/r)$ in the prediction (4.4) must strongly modify the velocity profile.

Finally, the turbulent regime exhibits a large range on which the velocity field satisfies the predicted Keplerian rotation rate, with $q = 3/2$. Such Keplerian profiles are very different from what is observed in Taylor–Couette flows at large Reynolds number. In the latter, once both the bulk flow and the radial boundary layers are turbulent, the differential rotation remains generally confined close to the radial boundaries, and the bulk flow exhibits a flat profile. The persistence of a mean Keplerian profile $u_\theta \propto 1/\sqrt{r}$ in the bulk flow comes from the volumic Lorentz force driving the flow, absent in boundary-driven Taylor–Couette (TC) flows (Avila 2012; Lopez & Avila 2017).

Figure 9(a) (respectively figure 9b) shows radial profiles of the mean azimuthal velocity field obtained from potential probes (respectively Doppler velocimetry). First, the good agreement between the two types of measurement indicates that, at least in this regime, the vertical component of the velocity is negligible. In addition, it shows that the change in the velocity profile from marginal flows to Keplerian rotation rates appears smoothly when the current is increased at fixed magnetic field. Moreover, figure 9(b) focuses on the Keplerian regime only, and shows that once in the turbulent regime, the velocity profile remains completely unchanged (the current has been varied by an order of magnitude without noticing any change). This suggests some ultimate nature of this turbulent regime.

The term ultimate regime used here refers to the ultimate regime of thermal convection predicted by Kraichnan (1962), who used similar arguments to derive a law for heat transport in strongly turbulent flows. Because of the analogy between Rayleigh–Bénard convection and Taylor–Couette flows, an analogue ultimate regime has been extensively studied in rotating flows in a cylindrical geometry, see for instance Huisman *et al.* (2012). The evolution of the global angular momentum

$$L = \int_{r_{min}}^{r_{max}} r^2 \overline{u_\theta}(r) \, dr \quad (5.1)$$

is shown in figure 8(b) and clearly illustrates the existence of three different types of angular momentum transport. As in Taylor–Couette flows, the Keplerian regime can be regarded as an ultimate turbulent regime occurring only at very large Reynolds number and transporting very effectively the angular momentum outward.

This question of the angular momentum transport is crucial in astrophysics. As explained in the introduction, accretion discs around black holes and proto-stars are known to exhibit similar turbulent rotation profiles $\Omega \propto r^{-3/2}$ and exhibit very efficient angular momentum transport for reasons that are still unclear. Keplerian rotation rates can only be approached in Taylor–Couette experiments, and there is a fairly active debate as to whether or not such quasi-Keplerian flows are turbulent and efficient in transporting angular momentum at large Reynolds number (Ji *et al.* 2006; Eckhardt, Grossmann & Lohse 2007; Paoletti & Lathrop 2011; Avila 2012; Paoletti *et al.* 2012; Fromang & Lesur 2019). It is therefore interesting to obtain here a truly Keplerian flow, in a regime undoubtedly turbulent. Although the turbulence originates from mechanisms radically different from its astrophysical counterpart, the KEPLER experiment provides an interesting experimental analogue of a Keplerian accretion disc, at least regarding the angular momentum profiles, the aspect ratio and the presence of a magnetic field which are typical of these astrophysical objects. Naturally, the problem is quite different from the Taylor–Couette problem, mostly because of the presence of the volumetric Lorentz force driving the flow and the fact that the mean flow is Rayleigh stable. In particular, the KEPLER experiment is associated with

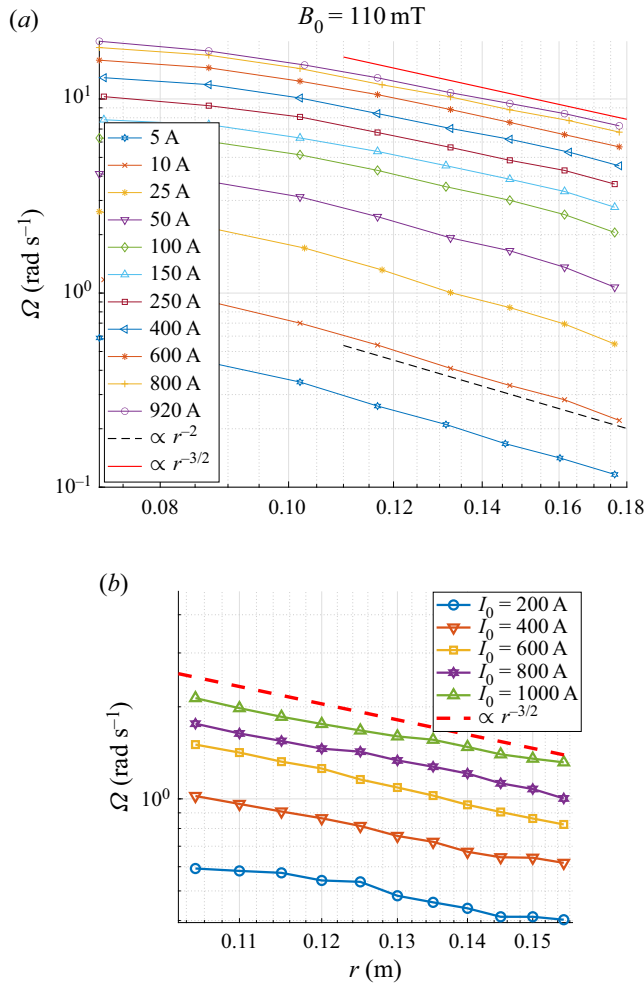


Figure 9. (a) Angular velocity obtained from potential probes for $B_0 = 110$ mT, for increasing current showing the transition from the laminar profile (4.1) (dashed black line) to Keplerian turbulent flows (4.8) (solid red line). (b) Angular velocity $\Omega(r)$ obtained from Doppler probes, for five values of injected current I (200, 400, 600, 800 and 1000 A). The dashed line corresponds to a power law $r^{-3/2}$. Here, $B_0 = 80$ mT, $Ha \sim 0.57B_0$.

a transverse current of azimuthal motion which is not conserved in the radial direction, contrary to classical set-ups. In this regard, the transport of angular momentum in our system is therefore more analogous to Rayleigh–Bénard convection with internal heating. A full discussion of this analogy and of the angular momentum transport in this experiment is thus beyond the scope of this paper, and will be reported in a forthcoming article.

6. Quasi-bidimensional turbulence

6.1. Power spectra and energy fluxes

The above results show that, at large forcing $I_0 B_0$, the flow is clearly turbulent. The dimensionality of this flow is, however, less trivial. Most previous experiments on similar electrically driven flows reported the generation of quasi-bidimensional turbulent flows at large magnetic field. There are, however, two important differences with the results

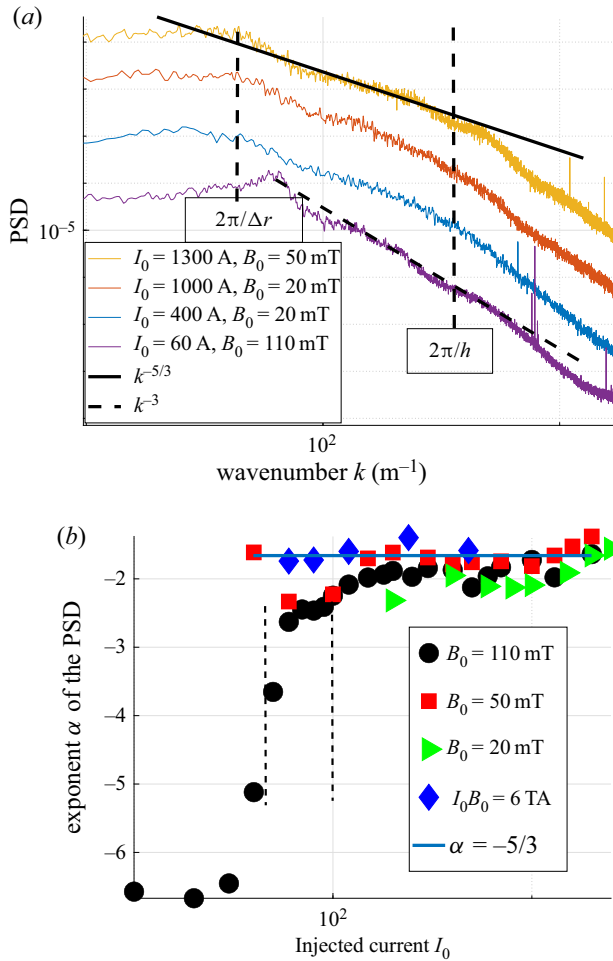


Figure 10. (a) Power spectral densities measured with the potential probes at four different points in the parameter space. The lines correspond to scalings $E(k) \propto k^{-5/3}$ and $E(k) \propto k^{-3}$. (b) Coefficient of the slope of the power spectral density as a function of the injected current I in the range: $k = [100-300]$. Here, $Ha \sim 0.57B_0$ with B_0 in mT.

reported here: our experiment operates at a significantly smaller interaction parameter N_I , and takes place in a very thin layer of thickness $h \ll \Delta r$, leading to a different regime.

Figure 10(a) shows typical examples of power spectra obtained in the turbulent regime. These spatial spectra were obtained from time series using a Taylor hypothesis based on the fact that the mean azimuthal flow is much larger than the fluctuations. Note that the four cases studied here are indicated by circles in figure 2.

In three of the four cases presented in figure 10, $Re > 1, 5 \times 10^5$, $R_B > 360$ and $\Lambda < 1$, such that they all belong to the turbulent regime described in the previous section, but the interaction parameter N_I remains between 0.25 and 16. Such values are much smaller than the ones used previously in similar experiments, but sufficiently large for quasi-2-D turbulence to be generated.

In all cases except for the low frequency region, the velocity field u_θ exhibits important turbulent fluctuations ($u'_\theta/\bar{u}_\theta \sim 10\%$) and all energy spectra computed at $B_0 < 100 \text{ mT}$ follow closely $E(f) \propto f^{-5/3}$ for $2\pi/\Delta r < k < 2\pi/h$ with a much steeper slope for

$k > 2\pi/h$. The latter can probably be attributed to the cutoff of the potential probes, which are limited by the finite distance l_p between the two electrodes measuring the local voltage and generate a $k^{-11/3}$ spectrum for wavenumbers $k > 2\pi/l_p$ (Berhanu *et al.* 2008). Figure 10(b) reports the slope α of the power spectral density (PSD) computed for wavenumbers $k = [100-300]$, which correspond to distances midway between the largest (horizontal) scale Δr and the smaller vertical scale h of the experiment. It shows that this $k^{-5/3}$ exponent is observed for a large range of the parameters (I_0, B_0) , and deviations from it occur only at very large field and small current.

This $k^{-5/3}$ spectrum could correspond either to a direct 3-D turbulent cascade of energy as predicted by Kolmogorov, or to the Kraichnan prediction of an inverse cascade of energy towards the large scales.

In order to access the energy flux characterizing the turbulent cascade, one can compute the third order structure functions of the velocity field defined by

$$S_3(\ell) = \langle (\mathbf{u}(\mathbf{x}, \ell + d\ell) - \mathbf{u}(\mathbf{x}, \ell))^3 \rangle_x, \tag{6.1}$$

where $\langle \dots \rangle_x$ denotes a spatial average. Since we do not have access to well resolved spatial measurements, we rather computed S_3 from very long time series of the velocity field acquired from the potential probes. To do so, we introduce the velocity increment $\delta\mathbf{u}(t, \tau) = \mathbf{u}(t + \tau) - \mathbf{u}(t)$ as the difference between the values of the flow velocity at time $t + \tau$ and t . One can then take advantage of the strong mean azimuthal flow to transform the quantity $S_3(\tau) = \langle \delta\mathbf{u}(t, \tau)^3 \rangle_t$ into $S_3(\ell)$ by use of the Taylor hypothesis $\ell = \tau \bar{u}_\theta$. Depending on the direction of the flux of energy (in the k -space), two different behaviours are possible: in 3-D turbulence, the famous Kolmogorov 4/5 law $S_3(\ell) = -\frac{4}{5}\epsilon\ell$ is expected from the injection scale to the viscous dissipation scale. In the case of an inverse cascade, Kraichnan rather predicted an inverse cascade towards large scale with a positive structure function $S_3(\ell) = -\frac{3}{2}\epsilon\ell$, where ϵ is now negative.

Figure 11 shows typical structure functions $S_3(\ell)$, obtained for the same set of parameters as for figure 10. They all correspond to different physical situations. For $B_0 = 20$ mT and $I_0 = 400$ A, the energy is injected at a scale slightly smaller than h . It then essentially cascades towards the large scales, as evidenced by the positive value of $S_3(\ell)$ and its linear dependence $S_3(\ell) \propto \ell$ in the range $\ell = [h - \Delta r]$. The corresponding $k^{-5/3}$ spectrum of the PSD therefore corresponds to an inverse cascade of energy as predicted by Kraichnan.

For larger forcings ($I_0B_0 = 20$ or $I_0B_0 = 65$), the structure functions now clearly exhibit negative values in the range $\ell = 1-30$ mm, and positive values for $\ell > 3$ cm. The injection energy presumably takes place at an intermediate scale, leading to a (limited) scale separation $\Delta r > \ell_{inj} > h$, which is typical of thin layer turbulence. The negative values of $S_3(\ell)$ are therefore the signature of a direct cascade of energy which takes place from ℓ_{inj} to smaller scale. On the other hand, some part of the energy also cascades upscale from ℓ_{inj} to Δr , as shown by the positive values of S_3 in this range. This split cascade of energy, in which the energy is injected at an intermediate scale $h < \ell_{inj} < \Delta r$ and cascades in both directions, is very similar to the one predicted for turbulence in very thin layers when the injection scale is much larger than the thickness h but much smaller than the largest scale (here Δr) (Celani, Musacchio & Vincenzi 2010; Xia *et al.* 2011; Benavides & Alexakis 2017). Here, the natural integral scale for the 3-D structures is the height of the disc, such that we expect ℓ_{inj} not too far from h . In this regime, the $k^{-5/3}$ spectrum of the PSD for $k > 2\pi h$ describes a forward cascade of energy, while the rest of the spectrum still corresponds to the inverse cascade. Note that, in thin layer turbulence, the forward cascade of energy at small scale is accompanied by a co-directional cascade of enstrophy

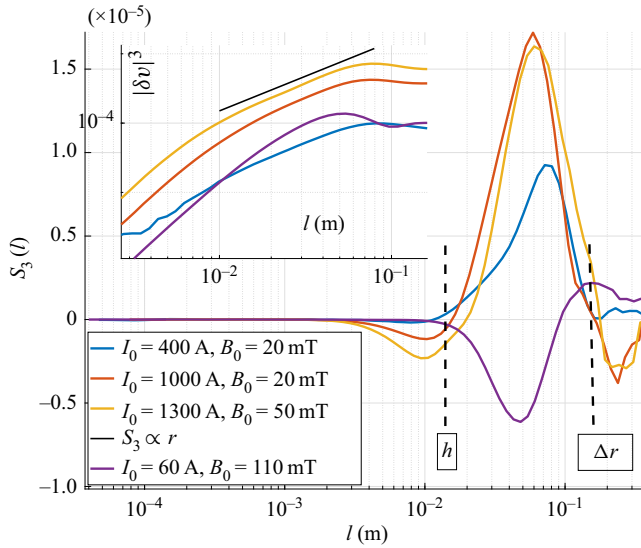


Figure 11. Structure function $S_3(l)$ at four different points in the parameter space. Inset: log–log plot of the modified structure functions $\langle |\delta v_L|^3 \rangle$. Here, $Ha \sim 0.57B_0$ with B_0 in mT.

in the range $[l_{inj} - h]$. This enstrophy spectrum is not visible in our data, probably because of the very limited scale separation of the experiment.

Finally, the regime observed at $B_0 = 110$ mT, $I_0 = 60$ A and reported in figures 10 and 11 obviously corresponds to a different regime than the double cascade described above. These parameters are located deep inside the regime of low frequency oscillations described in section 4.5. When this large scale instability occurs, it produces bi-dimensional vortices of the size of the gap $\ell \sim \Delta r$ which are advected by the mean flow and periodically passes through the probe. These vortices can be regarded as a type of condensate resulting from the inverse cascade (Sommeria 1986). The k^{-3} spectrum shown in figure 10 may therefore be a signature of this condensate, which takes the form of localized vortices travelling along the azimuthal direction.

This scenario is very different from the one given by Messadek *et al.*, where the k^{-3} spectrum is interpreted as an inverse cascade of energy modified by the strong Hartmann damping when the dissipation in the Hartmann layer is dominant at each wavenumber within the inertial range. We, however, emphasize that, because the low frequency oscillations strongly dominate the dynamics of the flow at large scale, the values of the structure function in the range $\ell = 1\text{--}10$ cm probably does not accurately describe the energy flux. It is then difficult to determine which of these scenarios is correct. In any case, this regime is associated with a very small energy flux at scales smaller than h .

6.2. Transition from direct to inverse cascade

In the recent years, the question of the transition from direct to inverse energy transfer in quasi-2-D systems has been at the centre of many studies, as summarized in the review of Alexakis & Biferale (2018). To follow the transition between these different regimes, we estimate the energy flux at a given scale ℓ^* by computing the quantity

$$\epsilon = - \left\langle \frac{S_3(\ell)}{\ell} \right\rangle, \tag{6.2}$$

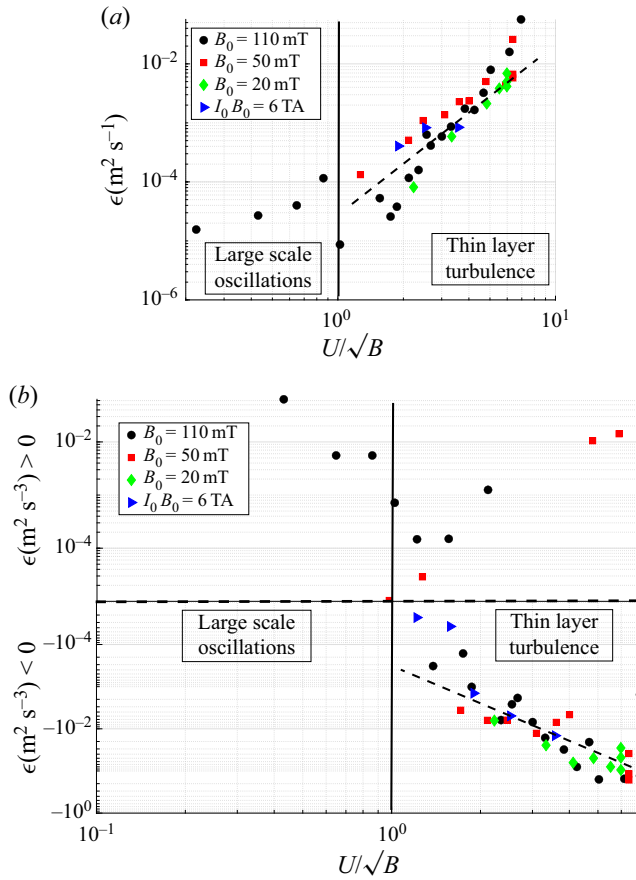


Figure 12. (a) Energy flux at large wavenumber ($\ell = [10^{-3} - 10^{-2}]$ m) as a function of $\bar{U}_\theta/\sqrt{B_0}$, showing a direct cascade of energy. (b) Energy flux at small wavenumber ($\ell = [10^{-2} - 10^{-1}]$ m) as a function of $\bar{U}_\theta/\sqrt{B_0}$, showing a transition from a direct to an inverse cascade of energy. The two black dashed lines correspond to the scaling $|\epsilon| \propto \bar{U}_\theta^3$. Here, $Ha \sim 0.57B_0$ with B_0 in mT.

where the average is taken on a given range of ℓ centred on ℓ^* . With this definition, a positive (respectively negative) value of ϵ corresponds to a flux of energy towards the small (respectively large) scales. Figure 12(a) shows the flux ϵ_f calculated on the range $\ell = 10^{-3} - 10^{-2}$ m at small scale, while figure 12(b) shows the flux ϵ_i calculated on the range $\ell = 10^{-2} - 10^{-1}$ m, at large scale. We plot this energy flux as a function of the ratio $\bar{U}_\theta/\sqrt{B_0}$ which rescales on a single curve the data obtained for different Hartmann numbers.

Two different states are clearly identified: the regime generated at $\bar{U}_\theta/\sqrt{B_0} < 1$ by the large scale oscillations of the flow is associated with a very weak flux of energy at small scale (figure 12a) and a condensate at large scale ($S_3 > 0$, see figure 12b). For $\bar{U}_\theta/\sqrt{B_0} > 1$, this regime is replaced by a state characteristic of thin layer turbulence: scales smaller than h are characterized by a direct cascade of energy ($\epsilon > 0$, see figure 12a). The energy flux strongly increases with the velocity, and seems to follow a turbulent scaling $\epsilon \propto \bar{U}_\theta^3$. At large scales $h < \ell < \Delta r$, the flux is negative in this regime, as expected for an inverse

cascade of energy and follows the same scaling $|\epsilon| \propto \bar{U}_\theta^3$ but with a larger amplitude: most of the injected energy cascades upscale.

At $\bar{U}_\theta/\sqrt{B_0} \approx 1$, a sharp bifurcation is observed between these two states. Although it describes a bifurcation between the condensate and some sort of thin layer turbulence, it is interesting to note that it takes the form of a second-order phase transition, similarly to what was observed in numerical shell models (Benavides & Alexakis 2017) for the transition between direct and inverse cascade.

7. Concluding remarks

The thin-disc geometry $h/\Delta r \sim 0.1$ of the KEPLER experiment, combined with the use of a very large applied current and a large horizontal size allows us to study regimes of electromagnetically driven flow previously unexplored. Three different regimes were observed, depending solely on the values of the interaction parameter N_t and the Reynolds number Re compared to their critical values $N_t^c \simeq 10$, $Re^c \simeq 9 \times 10^4$.

At large interaction parameter ($N_t > N_t^c$) but small Reynolds number ($Re < Re^c$), the Lorentz force is balanced by viscosity, leading to the classical laminar solution, in which the velocity is independent of the magnetic field at the lowest order. In our thin-disc geometry, this solution exhibits a marginally stable profile $\Omega \propto r^{-2}$.

At smaller interaction parameter ($N_t < N_t^c$) and moderate Reynolds number ($Re < Re^c$), this laminar solution bifurcates to a regime in which the Lorentz force is now balanced by inertia, leading to a non-trivial dependence $u_\theta \propto (IB)^{2/3} r^{-1/3} f(\Delta r/r)$. Although dominated by inertia, the azimuthal flow is still laminar, and strongly influenced by the laminar Hartmann–Bödewadt layers generated near the endcaps. The radial flow is non-negligible, especially near the boundaries, but the angular velocity $\Omega \propto r^{-4/3}$ corresponds to quasi-Keplerian rotation.

If the magnetic field remains moderate ($N_t < 10$), a transition to turbulence occurs at large Reynolds number ($Re > Re^c$). This regime $u_\theta \propto \sqrt{IB/r} \log(Re)$ is now fully driven by the turbulent Reynolds stress and relies on the turbulence of the Hartmann–Bödewadt boundary layers. For this reason, it may be regarded as a regime of strong turbulence, somehow analogous to the ultimate regime observed in Taylor–Couette flows. It shows strong fluctuating velocity field and an efficient transport of angular momentum. The velocity profile exhibits a true Keplerian rotation rate, in which the angular velocity is $\Omega \propto r^{-3/2}$. This regime provides a very interesting analogue of the flow in accretion discs, which can be roughly described as Keplerian turbulent flows in thin magnetized discs.

Finally, in the small region of the parameter space defined by $N_t > 10$, $Re > Re_c$, we report the existence of a large scale instability of the flow generating low-frequency perturbations at the largest scale $\ell_{inj} \approx 10$ cm. In this regime of bi-dimensional turbulence, third-order structure functions indicate that the energy mostly condensate at the largest available scale, with only very weak energy flux at small scale and fluctuations mostly confined in the horizontal plane.

On the contrary, the Keplerian turbulent regime is characterized by a quasi-bidimensional flow, in which the energy is injected at an intermediate scale $h < \ell_{inj} < \Delta r$. Because of the thin layer geometry, this injected energy also cascades towards the large horizontal scales. But in addition to this inverse cascade of energy, a direct forward cascade of energy towards scales smaller than h is also observed, reproducing the phenomenology expected in thin layer turbulence. Surprisingly, the transition from one regime to the other occurs quite abruptly, leading to a well-defined critical threshold for the occurrence of inverse (respectively direct) cascade of energy towards large (respectively small) scales.

From the astrophysical point of view, it is important to emphasize that the Kepler experiment is not a laboratory study of the magneto-rotational instability. Indeed, MRI experiments aim at generating turbulence from an hydrodynamically stable pre-existing Keplerian flow, while the Keplerian turbulence in our system results from the instability of top and bottom boundary layers. This active role of the vertical velocity gradient shares some interesting similarities with the vertical shear instability considered for weakly ionized accretion discs (Nelson, Gressel & Umurhan 2013). In consequence, the KEPLER experiment can rather be seen as an attempt to circumvent the current difficulties encountered by laboratory MRI experiments in generating magnetized Keplerian turbulence, in order to directly study the angular momentum transport or induction properties of accretion discs: the thin-disc geometry together with the use of a moderate magnetic field provides an interesting analogue to these astrophysical objects. In addition, the angular momentum is not injected at the radial boundaries of the system, but re-enforced in volume by the Lorentz force. Compared with classical Taylor–Couette flows, we believe that studying the detailed angular momentum transport in such a configuration may offer new insights on this matter for turbulent astrophysical flows. More precisely, the fact that a true Keplerian rotation rate can be obtained in a turbulent regime is a significant advantage compared with relatively stable quasi-Keplerian Taylor–Couette flows.

Finally, an appealing continuation of this work would be to design a larger version of the experiment for which the magneto-rotational instability is possibly accessible. Several remarks can be made on the feasibility of this. First, as the electromagnetic forcing involves no moving parts, it reduces the risk of leaks compared with classical Taylor–Couette set-ups. Using liquid sodium ($\mu_0\sigma = 12 \text{ s m}^{-2}$), a larger horizontal size ($L = 50 \text{ cm}$), and a slightly larger electromagnetic forcing ($I_0 = 5000 \text{ A}$ and $B_0 = 0.15 \text{ T}$), (4.8) yields a typical velocity of 6 m s^{-1} leading to $Rm \sim 40$, which may be sufficient for the observation of MRI. Note, however, that, in such configuration, the effect of the MRI would be to increase the angular momentum transport rather than triggering the turbulence. This means that the presence of turbulent fluctuations inherent to the generation of a Keplerian flow in our set-up may very well increase the onset through turbulent diffusion, or complicate the measurements of angular momentum transport induced by MRI. Besides strong induction effects, the MRI also requires that the applied magnetic field is not too strong, namely $k \cdot V_A < \Omega$ with $V_A = B_0/\sqrt{\mu_0\rho}$, the Alfvén velocity. As Ω decreases radially, this condition would be easily fulfilled, but only in the inner part of the flow. In this perspective, a numerical modelling of the experiment described here would be interesting, because it would clarify the critical onset for the occurrence of MRI, and help understanding of the various regimes described in this paper. Rather than using liquid sodium, our experiment can also be half-filled with liquid gallium, half-filled with mercury, thus providing a quasi-free surface condition for the bottom mercury (capillary length $l_c \sim 0.6 \text{ mm}$). For large currents, the azimuthal flow is expected to be an order of magnitude faster than the non-dispersive gravity waves generated at the gallium–mercury interface. This would provide an interesting shallow-water analogue of compressible turbulence in the presence of shock waves, a situation once again encountered in accretion discs and in the interstellar medium.

Acknowledgements. We thank A. Alexakis for useful discussions on 2-D turbulence, N. Garroum for his technical assistance and our anonymous referees for their very constructive input.

Funding. This work was supported by funding from the French program ‘JCJC’ managed by Agence Nationale de la Recherche (grant ANR 19-CE30-0025-01); the CEFLPRA contract 6104-1; and the Institut Universitaire de France.

Declaration of interests. The authors report no conflict of interest.

Author ORCIDs.

- ID M. Vernet <https://orcid.org/0000-0003-3128-0650>;
- ID M. Pereira <https://orcid.org/0000-0001-9122-4082>;
- ID S. Fauve <https://orcid.org/0000-0003-2379-6737>;
- ID C. Gissinger <https://orcid.org/0000-0002-1734-6716>.

REFERENCES

- ALEXAKIS, A. & BIFERALE, L. 2018 Cascades and transitions in turbulent flows. *Phys. Rep.* **767–769**, 1–101.
- AVILA, M. 2012 Stability and angular-momentum transport of fluid flows between corotating cylinders. *Phys. Rev. Lett.* **108**, 124501.
- BALBUS, S.A. & HAWLEY, J.F. 1991 A powerful local shear instability in weakly magnetized disks. I-Linear analysis. II-Nonlinear evolution. *Astrophys. J.* **376**, 214–233.
- BAYLIS, J.A. 1971 Experiments on laminar flow in curved channels of square section. *J. Fluid Mech.* **48**, 417–422.
- BAYLIS, J.A. & HUNT, J.C.R. 1971 MHD flow in an annular channel: theory and experiment. *J. Fluid Mech.* **48**, 423–428.
- BENAVIDES, S.J. & ALEXAKIS, A. 2017 Critical transitions in thin layer turbulence. *J. Fluid Mech.* **822**, 364–385.
- BERHANU, M., GALLET, B., MORDANT, N. & FAUVE, S. 2008 Reduction of velocity fluctuations in a turbulent flow of gallium by an external magnetic field. *Phys. Rev. E* **78**, 015302(R).
- BOISSON, J., KLOCHKO, A., DAVIAUD, F., PADILLA, V. & AUMAITRE, S. 2012 Travelling waves in a cylindrical magnetohydrodynamically forced flow. *Phys. Fluids* **24** (4), 044101.
- BOISSON, J., MONCHAUX, R. & AUMAITRE, S. 2017 Inertial regimes in a curved electromagnetically forced flow. *J. Fluids Mech.* **813**, 860–881.
- CELANI, A., MUSACCHIO, S. & VINCENZI, D. 2010 Turbulence in more than two and less than three dimensions. *Phys. Rev. Lett.* **104** (18), 184506.
- DAVIDSON, P.A. & POTHERAT, A. 2002 A note on Bodewadt–Hartmann layers. *Eur. J. Mech. B/Fluids* **21**, 545–559.
- DUBRULLE, B., MARIE, L., NORMAND, C., RICHARD, D., HERSANT, F. & ZAHN, J.-P. 2005 A hydrodynamic shear instability in stratified disks. *Astron. Astrophys.* **429** (1), 1–13.
- ECKHARDT, B., GROSSMANN, S. & LOHSE, D. 2007 Torque scaling in turbulent Taylor–Couette flow between independently rotating cylinders. *J. Fluid Mech.* **581**, 221–250.
- FROMANG, S. & LESUR, G.R.J. 2019 Angular momentum transport in accretion disks: a hydrodynamical perspective. *Astro Fluid* **82**, 391–413.
- HUISMAN, S.G., VAN GILS, D.P.M., GROSSMANN, S., SUN, C. & LOHSE, D. 2012 Ultimate turbulent Taylor–Couette flow. *Phys. Rev. Lett.* **108**, 024501.
- HUNT, J.C.R. 1965 Magnetohydrodynamic flow in rectangular ducts. *J. Fluid Mech.* **21** (4), 577–590.
- HARTMANN, J. & LAZARUS, F. 1937 Experimental investigations on the flow of mercury in a homogeneous magnetic field. *K. Dan. Vidensk. Selsk. Mat. Fys. Medd.* **15** (7), 1–45.
- JI, H., BURIN, M., SCHARTMAN, E. & GOODMAN, J. 2006 Hydrodynamic turbulence cannot transport angular momentum effectively in astrophysical disks. *Nature* **444** (7117), 343–346.
- KHALZOV, I.V., SMOLYAKOV, A.I. & ILGISONIS, V.I. 2010 Equilibrium magnetohydrodynamic flows of liquid metals in magnetorotational instability experiments. *J. Fluid Mech.* **644**, 257–280.
- KRAICHNAN, J.R.H. 1962 Turbulent thermal convection at arbitrary Prandtl number. *Phys. Fluids* **5**, 1374–1389.
- KRASNOV, D.S., ZIENICKE, E., ZIKANOV, O., BOECK, T. & THESS, A. 2004 Numerical study of the instability of the Hartmann layer. *J. Fluid Mech.* **504**, 183–211.
- LESUR, G. & LONGARETTI, P.-Y. 2005 On the relevance of subcritical hydrodynamic turbulence to accretion disk transport. *Astron. Astrophys.* **444** (1), 25–44.
- LESUR, G.R.J. 2021 Magnetohydrodynamics of protoplanetary discs. *J. Plasma Phys.* **87**, 205870101.
- LOPEZ, J.M. & AVILA, M. 2017 Boundary-layer turbulence in experiments on quasi-Keplerian flows. *J. Fluid Mech.* **817**, 21–34.
- MESSADEK, K. & MOREAU, R. 2002 An experimental investigation of MHD quasi-two-dimensional turbulent shear flows. *J. Fluid Mech.* **456**, 137–159.

- MOFFATT, K. 1961 The amplification of a weak applied magnetic field by turbulence in fluids of moderate conductivity. *J. Fluid Mech.* **11**, 625–635.
- MORESCO, P. & ALBOUSSIÈRE, T. 2004a Experimental study of the instability of the Hartmann layer. *J. Fluid Mech.* **504**, 167–181.
- MORESCO, P. & ALBOUSSIÈRE, T. 2004b Stability of Bödewadt–Hartmann layers. *Eur. J. Mech. B/Fluids* **23** (6), 851–859.
- MURGATROYD, W. 1953 Experiments on magneto-hydrodynamic channel flow. *Phil. Mag.* **44**, 1348–1354.
- NELSON, R.P., GRESSEL, O. & UMURHAN, O.M. 2013 Linear and non-linear evolution of the vertical shear instability in accretion discs. *Mon. Not. R. Astron. Soc.* **435** (3), 2610–2632.
- PAOLETTI, M.S., VAN GILS, D.P.M., DUBRULLE, B., SUN, C., LOHSE, D. & LATHROP, D.P. 2012 Angular momentum transport and turbulence in laboratory models of keplerian flows. *Astron. Astrophys.* **547**, A64.
- PAOLETTI, M.S. & LATHROP, D.P. 2011 Angular momentum transport in turbulent flow between independently rotating cylinders. *Phys. Rev. Lett.* **106**, 024501.
- POTHERAT, A. 2007 Quasi-two-dimensional perturbations in duct flows under transverse magnetic field. *Phys. Fluids* **19** (7), 074104.
- POTHERAT, A. 2012 Three-dimensionality in quasi-two-dimensional flows: recirculations and barrel effects. *Europhys. Lett.* **98** (6), 64003.
- POTHERAT, A. & KLEIN, R. 2014 Why, how and when MHD turbulence at low RM becomes three-dimensional. *J. Fluid Mech.* **761**, 168–205.
- POTHERAT, A., SOMMERIA, J. & MOREAU, R. 2000 An effective two-dimensional model for MHD flows with transverse magnetic field. *J. Fluid Mech.* **424**, 75–100.
- POYE, A., AGULLO, O., PLIHON, N., BOS, W.J.T., DESANGLES, V. & BOUSSELIN, G. 2020 Scaling laws in axisymmetric magnetohydrodynamic duct flows. *Phys. Rev. Fluids* **5**, 043701.
- RAYLEIGH, L. 1917 On the dynamics of revolving fluids. *Proc. R. Soc. Lond. A* **93** (648), 148–154.
- REDDY, K.S., FAUVE, S. & GISSINGER, C. 2018 Instabilities of MHD flows driven by traveling magnetic fields. *Phys. Rev. Fluids* **3**, 063703.
- ROACH, A.H., SPENCE, E.J., GISSINGER, C., EDLUND, E.M., SLOBODA, P., GOODMAN, J. & JI, H. 2012 Observation of a free-Shercliff-layer instability in cylindrical geometry. *Phys. Rev. Lett.* **108**, 154502.
- SISAN, D.R., MUJICA, N., TILLOTSON, W.A., HUANG, Y.-M., DORLAND, W., HASSAM, A.B., ANTONSEN, T.M. & LATHROP, D.P. 2004 Experimental observation and characterization of the magnetorotational instability. *Phys. Rev. Lett.* **93**, 114502.
- SOMMERIA, J. 1986 Experimental study of the two-dimensional inverse energy cascade in a square box. *J. Fluid Mech.* **170**, 139–168.
- SOMMERIA, J. & MOREAU, R. 1982 Why, how, and when, MHD turbulence becomes two-dimensional. *J. Fluid Mech.* **118**, 507–518.
- STEFANI, F. & GERBETH, G. 2004 MRI in Taylor–Dean flows. *AIP Conf. Proc.* **733**, 100.
- STEFANI, F., GUNDRUM, T., GERBETH, G., RUDIGER, G., SCHULTZ, M., SZKLARSKI, J. & HOLLERBACH, R. 2006 Experimental evidence for magnetorotational instability in a Taylor–Couette flow under the influence of a helical magnetic field. *Phys. Rev. Lett.* **97**, 184502.
- STELZER, Z., CEBRON, D., MIRALLES, S., VANTIEGHEM, S., NOIR, J., SCARFE, P. & JACKSON, A. 2015a Experimental and numerical study of electrically driven magnetohydrodynamic flow in a modified cylindrical annulus. I. Base flow. *Phys. Fluids* **27** (7), 077101.
- STELZER, Z., MIRALLES, S., CEBRON, D., NOIR, J., VANTIEGHEM, S. & JACKSON, A. 2015b Experimental and numerical study of electrically driven magnetohydrodynamic flow in a modified cylindrical annulus. II. Instabilities. *Phys. Fluids* **27** (8), 084108.
- TABELING, P. & CHABRERIE, J.P. 1981 Magnetohydrodynamic Taylor vortex flow under a transverse pressure gradient. *Phys. Fluids* **24** (3), 406–412.
- VELIKHOV, E.P., IVANOV, A.A., ZAKHAROV, S.V., ZAKHAROV, V.S., LIVADNY, A.O. & SEREBRENNIKOV, K.S. 2006 Equilibrium of current driven rotating liquid metal. *Phys. Lett. A* **358** (3), 216–221.
- WINARTO, H., JI, H., GOODMAN, J., EBRAHIMI, F., GILSON, E. & WANG, Y. 2020 Parameter space mapping of the Princeton magnetorotational instability experiment. *Phys. Rev. E* **102**, 023113.
- XIA, H., BYRNE, D., FALKOVICH, G. & SHATS, M. 2011 Upscale energy transfer in thick turbulent fluid layers. *Nat. Phys.* **7** (4), 321–324.
- ZHAO, Y., ZIKANOV, O. & KRASNOV, D. 2011 Instability of magnetohydrodynamic flow in an annular channel at high Hartmann number. *Phys. Fluids* **23** (8), 084103.
- ZHAO, Y., ZIKANOV, O. & KRASNOV, D. 2012 Instabilities and turbulence in magnetohydrodynamic flow in a toroidal duct prior to transition in Hartmann layers. *J. Fluids Mech.* **692**, 288–316.